J Math Imaging Vis (2010) 37: 98–111
DOI 10.1007/s10851-010-0195-5

Multiphase Soft Segmentation with Total Variation and H^1 Regularization

Fang Li · Chaomin Shen · Chunming Li

Published online: 25 February 2010

Abstract In this paper, we propose a variational soft segmentation framework inspired by the level set formulation of multiphase Chan-Vese model. We use soft membership functions valued in [0, 1] to replace the Heaviside functions of level sets (or characteristic functions) such that we get a representation of regions by soft membership functions which automatically satisfies the sum to one constraint. We give general formulas for arbitrary N-phase segmentation, in contrast to Chan-Vese's level set method only 2^m-phase are studied. To ensure smoothness on membership functions, both total variation (TV) regularization and H^1 regularization used as two choices for the definition of regularization term. TV regularization has geometric meaning which requires that the segmentation curve length as short as possible, while H^1 regularization has no explicit geometric meaning but is easier to implement with less parameters and has higher tolerance to noise. Fast numerical schemes are designed for both of the regularization methods. By changing the distance function, the proposed segmentation framework can be easily extended to the segmentation of other types of images. Numerical results on cartoon images, piecewise smooth images and texture images demonstrate that our methods are effective in multiphase image segmentation.

F. Li (✉)
Department of Mathematics, East China Normal University, Shanghai, China
e-mail: fli@math.ecnu.edu.cn

C. Shen
Department of Computer Science, East China Normal University, Shanghai, China

C. Li
Institute of Imaging Science, Vanderbilt University, Nashville, TN 37232, USA

Keywords Chan-Vese model · Level set · Total variation regularization · H^1 regularization · Soft membership function

1 Introduction

Image segmentation is fundamental in computer vision. The aim is to partition an image into several regions so that the image within each region has uniform characteristics such as edges, intensities, color and texture. Image segmentation is extensively studied by variational methods and partial differential equations (PDE) in the past two decades [3, 19, 21, 29]. Snake [13] and geodesic active contour [3] models use edge detection functions and evolve the curve towards sharp gradient. However, the edge based method is sensitive to noise and therefore so a smoothing process is usually needed. Region based methods incorporate region and boundary information and are robust to noise. One of the most famous region based methods is the Mumford-Shah model [19], which approximates an image by piecewise smooth function with regular boundaries. It is difficult to implement the Mumford-Shad model in practice. The special case of piecewise constant Mumford-Shah model is studied by Chan and Vese in [4] and [5] using level set methods [20, 24]. The advantage of using the level set method is that it is easy to formulate the regularization term. However, the computation is somewhat expensive. Zhu et al. [29] proposed a region competition method unifying snake, region growing and Bayesian statistics. The model penalizes the length of the boundaries and the Bayesian error estimated by parametric probability distributions such as Gaussian distribution within each region. Then piecewise constant Mumford-Shah model can be regarded as a special case of the region competition method.

Multiphase segmentation is a more challenging problem than two-phase segmentation. The main difficulty lies in the effective representation of the regions and their boundaries. There are several recent works related to the multiphase Mumford-Shah model. Vese et al. [27] generalized the two-phase model [4] to multiphase segmentation by using multi level sets. Both piecewise constant and piecewise smooth cases are studied. The advantage of using level sets to represent the multi regions is that it automatically avoids the problems of vacuum and overlap. Lie at al. [16] proposed to use piecewise constant level set function in piecewise constant Mumford-Shah model. The interfaces between regions are represented by the discontinuities of the function. A smooth convex functional with a quadratic constraint needs to be minimized. Jung et al. [12] proposed a phase field method to handle multiphase piecewise constant segmentation. The method is based on the phase transition model of Modica and Mortola with a sinusoidal potential. Since the model is not quadratic or convex, a convex-concave procedure is used in the implementation.

Different from the above mentioned methods which yield hard segmentation result, soft (fuzzy) segmentation approaches are popular in data mining and medical image segmentation [1, 28]. The soft segmentation method assumes that each image pixel can be in several regions and the probability in each region is represented by soft membership function valued in $[0, 1]$. Recently, many two-phase soft segmentation models are proposed [2, 6, 10, 17, 18], in which one soft membership function is used in the functionals such that the functionals are convex with respect to the membership. The convexity ensures that the new methods are not sensitive to initialization and global minima can be found. Another advantage is that Chambolle's fast dual projection method [7] can be adopted in the implementation. Recently, the split Bregman method is introduced to solve the two-phase soft segmentation problem in [9] which is also fast. However, only two-phase segmentation are studied. A general multiphase stochastic variational soft segmentation model was proposed by Shen [26] based on the Mumford-Shah model. The author used a double well potential related to phase field to regularize the soft membership functions. The energy functional in this model is nonconvex with respect to each membership function. Numerically, a set of PDEs has to be solved with the gradient descent method, which makes the implementation computationally expensive.

In this paper, we propose a variational soft segmentation framework inspired by the level set formulation of multiphase Chan-Vese model. We use soft membership functions valued in $[0, 1]$ to replace the Heaviside functions of level sets such that we get a representation of regions by soft membership functions which automatically satisfies the sum to one constraint. Meanwhile, to ensure the smoothness of membership, both TV regularization and H^1 regularization are considered. TV regularization has geometric meaning which requires that the segmentation curve length as short as possible, while H^1 regularization has no explicit geometric meaning but is easier to implement with less parameters and has higher tolerance to noise. Fast numerical schemes are designed for the two regularization methods. By changing the distance function, the proposed segmentation framework can be easily extended such that we can handle different kinds of images. Numerical results on cartoon images, piecewise smooth images and texture images demonstrate that our methods are effective in multiphase image segmentation.

The outline of this paper is as follows. In Sect. 2, we propose and analyze our models. In Sect. 3, we present fast algorithms for both models. In Sect. 4, other distance functions are introduced to deal with piecewise smooth, texture and color images. In Sect. 5, experimental results are presented to illustrate the effectiveness of our model. Finally, we conclude the paper in Sect. 6.

2 The Proposed Method and Mathematical Analysis

First we consider the special case for 2^m-phase segmentation with m characteristic functions. We assume $\{\Omega_i\}_{i=1}^m$ be m subsets of image domain Ω, and $\mathbf{1}_{\Omega_i}$ be the characteristic function of region Ω_i. Then we can take use of $\{\mathbf{1}_{\Omega_i}\}_{i=1}^m$ to split the image domain into 2^m disjoint regions as follows. For $k = 1, 2, \dots, 2^m$, let $b_1^{m,k-1}, b_2^{m,k-1}, \dots, b_m^{m,k-1}$ be the binary representation of $k-1$ with m numbers, $b_i^{m,k-1} = 0 \vee 1, i = 1, 2, \dots, m$. Define $s_k^m = \sum_{i=1}^m b_i^{m,k-1}$, then

$$M_k^{2^m} = (-1)^{s_k^m} \prod_{i=1}^m (\mathbf{1}_{\Omega_i} - b_i^{m,k-1}) \tag{1}$$

is the characteristic function of the k-th region D_k, i.e., $M_k = \mathbf{1}_{D_k}$. It is easy to verify that $\bigcup_{k=1}^{2^m} D_k = \Omega$ and $D_{k_1} \cap D_{k_2} = \emptyset$ for any $k_1 \neq k_2, k_1, k_2 = 1, \dots, 2^m$. Therefore, $\{D_k\}_{k=1}^{2^m}$ is a partition of the image domain.

Let us first consider the piecewise constant image segmentation model whose idea is to approximate the image by a piecewise constant function, i.e.,

$$I \approx \sum_{k=1}^N c_k \mathbf{1}_{D_k}.$$

To solve this problem, a classical criterion developed in [19] is to minimize

$$\sum_{k=1}^N \mathrm{Per}(\partial D_k) + \lambda \int_\Omega \left(I - \sum_{k=1}^N c_k \mathbf{1}_{D_k} \right)^2 dx$$

where $\mathrm{Per}(\partial D_k)$ denotes the length of the boundary ∂D_k and $\lambda > 0$ is a weight to balance the two terms. Equivalently, we can minimize

$$\sum_{i=1}^{N} \mathrm{Per}(\partial\Omega_i) + \lambda \sum_{k=1}^{N} \int_\Omega (I - c_k)^2 \mathbf{1}_{D_k} dx.$$

In the case of $N = 2^m$, Chan and Vese used m level set functions $\phi_i : \Omega \to \mathbb{R}, i = 1, \dots, m$, such that

$$\begin{cases} \phi_i(x) > 0 & \text{if } x \in \Omega_i, \\ \phi_i(x) = 0 & \text{if } x \in \partial\Omega_i, \\ \phi_i(x) < 0 & \text{if } x \in \bar{\Omega}_i^{\,c}. \end{cases}$$

Therefore $\mathbf{1}_{\Omega_i} = H(\phi_i)$ where $H(\phi_i)$ is the Heaviside function: $H(\phi_i) = 1$ if $\phi_i \geq 0$ and $H(\phi_i) = 0$ otherwise. With m level sets, Chan-Vese energy functional is

$$E(\{\phi_i\}_{i=1}^m, \{c_k\}_{k=1}^{2^m}) = \sum_{i=1}^{m} \int_\Omega |\nabla H(\phi_i)| dx + \lambda \sum_{k=1}^{2^m} \int_\Omega |I - c_k|^2 M_k^{2^m} dx \tag{2}$$

where

$$M_k^{2^m} = (-1)^{s_k^m} \prod_{i=1}^{m} (H(\phi_i) - b_i^{m,k-1}). \tag{3}$$

Specially, if $N = 4, m = 2$, by formula (1), we have $M_1^4 = H(\phi_1)H(\phi_2)$, $M_2^4 = H(\phi_1)(1 - H(\phi_2))$, $M_3^4 = (1 - H(\phi_1))H(\phi_2)$, $M_4^4 = (1 - H(\phi_1))(1 - H(\phi_2))$. Remark that only 2^m-phase segmentation are studied by Chan and Vese.

In the numerical implementation, $H(\phi_i)$ is replaced by a smoothed version $H_\epsilon(\phi_i)$. Inspired by this, we propose to use soft smooth membership function $u_i \in [0, 1]$ to replace $\mathbf{1}_{\Omega_i}$. Now we consider a general N-phase segmentation problem, if $2^{m-1} < N \leq 2^m$, then we propose to solve the segmentation problem by minimizing the energy

$$E_1(\{u_i\}_{i=1}^m, \{c_k\}_{k=1}^N) = \sum_{i=1}^{m} \int_\Omega |\nabla u_i| dx + \lambda \sum_{k=1}^{N} \int_\Omega |I - c_k|^2 M_k^N dx \tag{4}$$

where if $N = 2^m$,

$$M_k^{2^m} = (-1)^{s_k^m} \prod_{i=1}^{m} (u_i - b_i^{m,k-1}). \tag{5}$$

Otherwise, if $2^{m-1} < N < 2^m$,

$$\begin{cases} M_k^N = (-1)^{s_k^m} \prod_{i=1}^m (u_i - b_i^{m,k-1}), \\ \quad \text{for } k = 1, \dots, 2k_0 \\ M_k^N = (-1)^{s_{k_1}^{m_1}} \prod_{i=1}^{m_1} (u_i - b_i^{m_1,k_1-1}), \\ \quad \text{for } k = 2k_0 + 1, \dots, N \end{cases} \tag{6}$$

where $m_1 = m - 1, k_0 = N - 2^{m_1}, k_1 = k - k_0$. More intuitively, we give the formulas of M_i^N for $N = 2, 3, 4, 5, 7, 8$ respectively.

$$\begin{aligned}
&2 \; \{ \; M_1^2 = u_1, \quad M_2^2 = 1 - u_1; \\
&3 \; \{ \; M_1^3 = u_1 u_2, \quad M_2^3 = u_1(1 - u_2), \quad M_3^3 = 1 - u_1; \\
&4 \begin{cases} M_1^4 = u_1 u_2, \quad M_2^4 = u_1(1 - u_2), \\ M_3^4 = (1 - u_1)u_2, \quad M_4^4 = (1 - u_1)(1 - u_2); \end{cases} \\
&5 \begin{cases} M_1^5 = u_1 u_2 u_3, \quad M_2^5 = u_1 u_2(1 - u_3), \\ M_3^5 = u_1(1 - u_2), \quad M_4^5 = (1 - u_1)u_2, \\ M_5^5 = (1 - u_1)(1 - u_2); \end{cases} \\
&7 \begin{cases} M_1^7 = u_1 u_2 u_3, \quad M_2^7 = u_1 u_2(1 - u_3), \\ M_3^7 = u_1(1 - u_2)u_3, \quad M_4^7 = u_1(1 - u_2)(1 - u_3), \\ M_5^7 = (1 - u_1)u_2 u_3, \quad M_6^7 = (1 - u_1)u_2(1 - u_3), \\ M_7^7 = (1 - u_1)(1 - u_2); \end{cases} \\
&8 \begin{cases} M_1^8 = u_1 u_2 u_3, \quad M_2^8 = u_1 u_2(1 - u_3), \\ M_3^8 = u_1(1 - u_2)u_3, \quad M_4^8 = u_1(1 - u_2)(1 - u_3), \\ M_5^8 = (1 - u_1)u_2 u_3, \quad M_6^8 = (1 - u_1)u_2(1 - u_3), \\ M_7^8 = (1 - u_1)(1 - u_2)u_3, \\ M_8^8 = (1 - u_1)(1 - u_2)(1 - u_3). \end{cases}
\end{aligned}$$

Remark that in the existing soft segmentation models such as [1, 26], they require that the soft membership functions satisfy two constraints: each membership function valued in $[0, 1]$ and the summation of all membership functions be one. It is usually a difficult task to handle the sum to one constraint. By design, with the formulas (5) and (6), the proposed soft membership functions automatically satisfies sum to one constraint, i.e., $\sum_{i=1}^N M_k = 1$.

The total variation term in E_1 ensures some regularity of membership function u_i. For more smoothness, H^1 regularity should be considered which results in our second energy

$$E_2(\{u_i\}_{i=1}^m, \{c_k\}_{k=1}^N) = \frac{1}{2} \sum_{i=1}^{m} \int_\Omega |\nabla u_i|^2 dx + \lambda \sum_{k=1}^{N} \int_\Omega |I - c_k|^2 M_k^N dx. \tag{7}$$

In the following, we will prove the existence of minimizer of the proposed energy functionals.

We fix N and therefore m. For simplicity, we use the notations $M_k = M_k^N$, $\mathbf{U} = \{u_i\}_{i=1}^m$ and $\mathbf{c} = \{c_k\}_{k=1}^N$. Then

$$E_1(\mathbf{U}, \mathbf{c}) = \sum_{i=1}^{m} \int_\Omega |\nabla u_i| dx + \lambda \sum_{k=1}^{N} \int_\Omega |I - c_k|^2 M_k dx. \tag{8}$$

Under the assumption that the image $I \in L^\infty(\Omega)$, the energy $E_1(\mathbf{U}, \mathbf{c})$ is well defined and finite for the admissible set $(\mathbf{U}, \mathbf{c}) \in BV_{[0,1]}(\Omega)^m \times \mathbb{R}^N$ where $BV_{[0,1]}(\Omega)$ denotes bounded variation (BV) functions valued in $[0, 1]$.

Theorem 1 (Existence of Minimizer to E_1) *Assume the image $I \in L^\infty(\Omega)$. Then for fixed parameters $N, \lambda > 0$, there exists a minimizer of the energy E_1 in $BV_{[0,1]}(\Omega)^m \times \mathbb{R}^N$.*

Proof Let $u_1 = 1$, $u_i = 0$, $i = 2, \dots, m$, then there exist some $1 \le k \le N$ such that $M_k = 1$ and $M_j = 0, \forall j \ne k$. Hence $c_k = \int_\Omega I dx/|\Omega|$ and $c_j = 0, \forall j \ne k$, then $E_1(\mathbf{U}, \mathbf{c}) = \int_\Omega (I - c_k)^2 dx < \infty$. Therefore the infimum of the energy must be finite. Let $(\mathbf{U}^n, \mathbf{c}^n) \subseteq BV_{[0,1]}(\Omega)^m \times \mathbb{R}^N$ be a minimizing sequence for energy E_1, that is, $E(\mathbf{U}^n, \mathbf{c}^n) \to \inf E(\mathbf{U}, \mathbf{c})$ as $n \to \infty$. Then there exists a constant $C > 0$, such that

$$E(\mathbf{U}^n, \mathbf{c}^n) = \sum_{i=1}^m \int_\Omega |\nabla u_i^n| dx + \sum_{k=1}^N \lambda \int_\Omega (I - c_k^n)^2 M_k^n dx \le C.$$

Then we have

$$\int_\Omega |\nabla u_i^n| dx \le C. \tag{9}$$

Since $u_i^n \in [0, 1]$, $\|u_i^n\|_{L^1(\Omega)} = \int_\Omega u_i^n dx \le |\Omega|$. Together with (9) we get (u_i^n) is uniformly bounded in $BV(\Omega)$ for each $i = 1, \dots, m$. By the compactness property of BV space, up to a subsequence also denoted by (u_i^n) after relabeling, there exists a function $u_i^* \in BV(\Omega)$ such that

$$u_i^n \to u_i^* \quad \text{strongly in } L^1(\Omega),$$
$$u_i^n \to u_i^* \quad \text{a.e. } x \in \Omega,$$
$$\nabla u_i^n \rightharpoonup \nabla u_i^* \quad \text{in the sense of measure.}$$

Then by the lower semicontinuity of total variation,

$$\int_\Omega |\nabla u_i^*| dx \le \liminf_{n \to \infty} \int_\Omega |\nabla u_i^n| dx. \tag{10}$$

Meanwhile since $u_i^n \in [0, 1]$, we get $u_i^* \in [0, 1]$.

It is easy to derive from the Euler-Lagrange equation of energy E that

$$c_k^n = \frac{\int_\Omega I(x) M_k^n(x) dx}{\int_\Omega M_k^n(x) dx}. \tag{11}$$

Since $M_k^n \in [0, 1]$, we have

$$|c_k^n| \le \|I\|_\infty.$$

By the boundedness of sequence $\{c_k^n\}$, we can abstract a subsequence also denoted by $\{c_k^n\}$ and a constant c_k^* such that

$$c_k^n \to c_k^*.$$

Finally, since $u_i^n \to u_i^*$, a.e. $x \in \Omega$ and $c_k^n \to c_k^*$, Fatou Lemma gives

$$\int_\Omega (I - c_k^*)^2 M_k^* dx \le \liminf_{n \to \infty} \int_\Omega (I - c_k^n)^2 M_k^n dx \tag{12}$$

where M_k^* is defined by M_k from replacing u_i in M_k by u_i^*. Combining inequalities (10) and (12) for all i and k, on a suitable subsequence, we have established that

$$E_1(\mathbf{U}^*, \mathbf{c}^*) \le \liminf_{n \to \infty} E_1(\mathbf{U}^n, \mathbf{c}^n) = \inf E_1(\mathbf{U}, \mathbf{c}), \tag{13}$$

and hence $(\mathbf{U}^*, \mathbf{c}^*)$ must be a minimizer. This completes the proof. □

By a similar argument using the compactness of Sobolev space $H^1(\Omega)$, we can prove the existence of minimizer of the energy E_2.

Theorem 2 (Existence of Minimizer to E_2) *Assume the image $I \in L^\infty(\Omega)$. Then for fixed parameters $N, \lambda > 0$, there exists a minimizer of the energy E_2 in $H^1_{[0,1]}(\Omega)^m \times \mathbb{R}^N$.*

3 Numerical Schemes

3.1 Minimizing E_1

We will derive a fast numerical method to handle the total variation term and the constraint $u_i \in [0, 1]$. For that end we add auxiliary variables $\mathbf{V} = \{v_i\}_{i=1}^m$ and approximate E_1 in (8) by

$$E_{1r}(\mathbf{U}, \mathbf{V}, \mathbf{c}) = \sum_{i=1}^m \int_\Omega |\nabla v_i| dx + \frac{1}{2\theta} \sum_{i=1}^m \int_\Omega (v_i - u_i)^2 dx + \lambda \sum_{k=1}^N \int_\Omega d_k M_k dx \tag{14}$$

where $d_k := |I - c_k|^2$ and θ is small enough to ensure that v_i approximates u_i in the sense of L^2 norm.

Since E_1 involves three groups of variables and E_1 is convex with respect to each variable u_i, v_i and c_k, alternative minimization method can be used to find the numerical solution.

3.1.1 *Minimization with Respect to* $\mathbf{c}$

Fixing $\mathbf{U}$ and $\mathbf{V}$, we calculate the derivative of E_{1r} with respect to c_k and set the result to zero, then we obtain

$$c_k = \frac{\int_\Omega I M_k dx}{\int_\Omega M_k dx}, \quad k = 1, \dots, N. \tag{15}$$

3.1.2 *Minimization with Respect to* $\mathbf{V}$

Fixing $\mathbf{U}$ and $\mathbf{c}$, the subproblem of v_i can be rewritten as

$$\min_{v_i} \int_\Omega |\nabla v_i| dx + \frac{1}{2\theta} \int_\Omega (v_i - u_i)^2 dx, \quad i = 1, \dots, m. \tag{16}$$

This is the well known Rudin-Osher-Fatemi (ROF) model [23]. Many newly proposed algorithms can solve this problem very fast, for example, Chambolle's duality projection method [7], the Split-Bregman (SB) method [8], Jia's method [11] which is a convergence formulation of SB and Shen's method [25]. Here we follow Shen's method in which the operator splitting method is used.

The corresponding Euler-Lagrange equation of problem (16) is

$$0 \in \partial(f \circ L)(v_i) + \frac{1}{\theta}(v_i - u_i). \tag{17}$$

By property of subgradient, $\partial(f \circ L)(v_i) = L^* \partial f(Lv_i)$. Define $L^*\mathbf{y}_i = L^*\partial f(Lv_i)$, then $\mathbf{y}_i \in \partial f(Lv_i)$ which is equivalent to $Lv_i \in \partial f^*(\mathbf{y}_i)$. Hence v_i satisfies (17) if and only if there exists an auxiliary variable $\mathbf{y}_i$, such that

$$0 \in L^*\mathbf{y}_i + \frac{1}{\theta}(v_i - u_i), \tag{18}$$

$$0 \in \partial f^*(\mathbf{y}_i) - Lv_i. \tag{19}$$

We can now apply the operator splitting method with scalar $\tau > 0$ to (19) and obtain two equations

$$0 \in \tau \partial f^*(\mathbf{y}_i) + \mathbf{y}_i - \mathbf{t}_i, \tag{20}$$

$$\mathbf{t}_i = \mathbf{y}_i + \tau L v_i. \tag{21}$$

(20) is also equivalent to

$$0 \in \tau \mathbf{y}_i + \partial f(\mathbf{y}_i - \mathbf{t}_i),$$

which is the optimality condition of

$$\min_{\mathbf{y}_i} \frac{\tau}{2}\|\mathbf{y}_i\|_2^2 + f(\mathbf{y}_i - \mathbf{t}). \tag{22}$$

It is easy to get that problem (22) has closed-form solution

$$\mathbf{y}_i = \min\left\{\|\mathbf{t}_i\|_2, \frac{1}{\tau}\right\} \frac{\mathbf{t}_i}{\|\mathbf{t}_i\|_2}. \tag{23}$$

Sum up (18), (21) and (23), the minimization problem (16) can be solved by the following alternative iteration:

$$v_i = u_i - \theta \nabla^T \mathbf{y}_i, \tag{24}$$

$$\mathbf{y}_i = \min\left\{\frac{1}{\tau}, \|\mathbf{y}_i + \tau \nabla v_i\|_2\right\} \frac{\mathbf{y}_i + \tau \nabla v_i}{\|\mathbf{y}_i + \tau \nabla v_i\|_2}. \tag{25}$$

3.1.3 Minimization with Respect to **U**

Fixing **V** and **c**, we consider the optimization problem

$$\min_U F(\mathbf{U}) = \frac{1}{2\theta} \sum_{i=1}^m \int_\Omega (v_i - u_i)^2 dx + \lambda \sum_{k=1}^N \int_\Omega d_k M_k dx \tag{26}$$

subject to

$$0 \le u_i \le 1, \quad i = 1, \ldots, m.$$

We use the notation $D^N := \sum_{k=1}^N d_k M_k$ and define $r_i^N := \frac{\partial D^N}{\partial u_i}$. By formulas of M_k in (5) and (6), we get that if $N = 2^m$,

$$r_i^{2^m} = \sum_{k=1}^{2^m} (-1)^{s_k^m} \prod_{j=1, j\neq i}^{m} (u_j - b_j^{m,k-1}), \quad i = 1, \ldots, m. \tag{27}$$

Otherwise, if $2^{m-1} < N < 2^m$, for $i = 1, \ldots, m_1$,

$$\begin{aligned} r_i^N = &\sum_{k=1}^{2k_0} (-1)^{s_k^m} \prod_{j=1, j\neq i}^{m} (u_j - b_j^{m,k-1}) \\ &+ \sum_{k=2k_0+1}^{N} (-1)^{s_{k_1}^{m_1}} \prod_{j=1, j\neq i}^{m_1} (u_j - b_j^{m_1,k_1-1}). \end{aligned} \tag{28}$$

For $i = m$,

$$r_m^N = \sum_{k=1}^{2k_0} (-1)^{s_k^m} \prod_{j=1, j\neq i}^{m} (u_j - b_j^{m,k-1}). \tag{29}$$

For the special case of $N = 3, 4, 5, 7, 8$, the detailed formulas of r_i^N are as follows:

$$3\begin{cases} r_1^3 = d_1 u_2 + d_2(1-u_2) - d_3, \\ r_2^3 = (d_1 - d_2)u_1; \end{cases}$$

$$4\begin{cases} r_1^4 = (d_1 - d_3)u_2 + (d_2 - d_4)(1-u_2), \\ r_2^4 = (d_1 - d_2)u_1 + (d_3 - d_4)(1-u_1); \end{cases}$$

$$5\begin{cases} r_1^5 = d_1 u_2 u_3 + d_2 u_2(1-u_3) + d_3(1-u_2) - d_4 u_2 \\ \qquad - d_5(1-u_2), \\ r_2^5 = d_1 u_1 u_3 + d_2 u_1(1-u_3) - d_3 u_1 + d_4(1-u_1) \\ \qquad - d_5(1-u_1), \\ r_3^5 = (d_1 - d_2)u_1 u_2; \end{cases}$$

$$7\begin{cases} r_1^7 = (d_1 - d_5)u_2 u_3 + (d_2 - d_6)u_2(1-u_3) \\ \qquad + d_3(1-u_2)u_3 + d_4(1-u_2)(1-u_3) \\ \qquad - d_7(1-u_2), \\ r_2^7 = (d_1 - d_3)u_1 u_3 + (d_2 - d_4)u_1(1-u_3) \\ \qquad + d_5(1-u_1)u_3 + d_6(1-u_1)(1-u_3) \\ \qquad - d_7(1-u_1), \\ r_3^7 = (d_1 - d_2)u_1 u_2 + (d_3 - d_4)u_1(1-u_2) \\ \qquad + (d_5 - d_6)(1-u_1)u_2; \end{cases}$$

$$8\begin{cases} r_1^8 = (d_1 - d_5)u_2 u_3 + (d_2 - d_6)u_2(1-u_3) \\ \qquad + (d_3 - d_7)(1-u_2)u_3 \\ \qquad + (d_4 - d_8)(1-u_2)(1-u_3), \\ r_2^8 = (d_1 - d_3)u_1 u_3 + (d_2 - d_4)u_1(1-u_3) \\ \qquad + (d_5 - d_7)(1-u_1)u_3 \\ \qquad + (d_6 - d_8)(1-u_1)(1-u_3), \\ r_3^8 = (d_1 - d_2)u_1 u_2 + (d_3 - d_4)u_1(1-u_2) \\ \qquad + (d_5 - d_6)(1-u_1)u_2 \\ \qquad + (d_7 - d_8)(1-u_1)(1-u_2). \end{cases}$$

We simplify r_i^N as r_i in the following.

There exists a unique global minimizer of problem (26) since the objective function is strictly convex and the feasible region is convex. Firstly, we derive the Euler-Lagrange equation of (26) without considering the constraints, then we obtain

$$\frac{1}{\theta}(u_i - v_i) + \lambda r_i = 0. \tag{30}$$

Hence

$$u_i = v_i - \lambda\theta r_i.$$

Secondly, we apply the constraints and define

$$\hat{u}_i := \min\{\max\{u_i, 0\}, 1\}. \tag{31}$$

We have the following claim:

Proposition 1 *By definition* (31), $\hat{U} = (\hat{u}_1, \dots, \hat{u}_n)$ *is the exact closed-form solution of problem* (26).

See the proof in the Appendix.

3.1.4 Algorithm Details

Based on (15), (24), (25) and (31), the algorithm can be summarized in the following four steps:

– Initialization: $u_1^0 = I/\max_\Omega(I)$, $u_i^0 (i = 2, \dots, m)$ be random matrices following uniform distribution at $[0, 1]$, $v_i^0 = u_i^0$, $c_i^0 = 0$, $\mathbf{y}_i = \mathbf{0}$ for $i = 1, \dots, m$.
– Iteration: for $i = 1, \dots, m$, $k = 1, \dots, N$, $n = 0, 1, 2, \dots$

$$c_k^{n+1} = \frac{\int_\Omega I M_k^n dx}{\int_\Omega M_k^n dx},$$

$$v_i^{n+1} = u_i^n - \theta \nabla^T \mathbf{y}_i^n,$$

$$\mathbf{y}_i^{n+1} = \min\left\{\frac{1}{\tau}, \|\mathbf{y}_i^n + \tau\nabla v_i^n\|_2\right\} \frac{\mathbf{y}_i^n + \tau\nabla v_i^n}{\|\mathbf{y}_i^n + \tau\nabla v_i^n\|_2},$$

$$u_i^{n+1} := \min\{\max\{v_i^n - \lambda\theta r_i^n, 0\}, 1\}.$$

– Termination criterion:

$$\|\mathbf{c}^{n+1} - \mathbf{c}^n\| \le \epsilon$$

where $\|\cdot\|$ denotes the Euclidean distance and ϵ is a small positive number defined by the user.

3.2 Minimizing E_2

Let us rewrite the problem as

$$\min_{u_i \in [0,1]} E_2(\mathbf{U}, \mathbf{c}) = \frac{1}{2}\sum_{i=1}^m \int_\Omega |\nabla u_i|^2 dx + \lambda \sum_{k=1}^N \int_\Omega |I - c_k|^2 M_k dx. \tag{32}$$

3.2.1 Minimization with Respect to c

It is obvious that minimizing E_2 with respect to **c** is the same as minimize E_1 with respect to **c**.

3.2.2 Minimization with Respect to U

Similar to the analysis of E_1, we can calculate the derivative of the distance term with respect to u_i, which is denoted as r_i. Then the Euler-Lagrange equation of E_2 with respect to u_i is given by

$$-\Delta u_i + \lambda r_i = 0. \tag{33}$$

A fast approximated solution is provided by a Gauss-Seidel iterative scheme, i.e.

$$(u_i)_{p,q} = \frac{1}{4}((u_i)_{p+1,q} + (u_i)_{p-1,q} + (u_i)_{p,q+1} + (u_i)_{p,q-1} - \lambda(r_i)_{p,q})$$

where p, q denote the grid. To handle the constraint, we can project the solution onto $[0, 1]$ as done in [9]. Thus, the solution is simplified as

$$\begin{aligned} u_i &= \frac{1}{4}(u_i^{so} + u_i^{no} + u_i^{ea} + u_i^{we} - \lambda r_i), \\ u_i &= \min\{\max\{u_i, 0\}, 1\}, \end{aligned} \tag{34}$$

where $u_i^{so}, u_i^{no}, u_i^{ea}, u_i^{we}$ means shift the matrix u_i one pixel in the south, north, east and west direction respectively.

3.2.3 Algorithm Details

Based on (15) and (34), the algorithm can be summarized in the following steps:

– Initialization: $u_1^0 = I/\max_\Omega(I)$, $u_i^0 (i = 2, \dots, m)$ be random matrices following uniform distribution at $[0, 1]$, $c_i^0 = 0$ for $i = 1, \dots, m$.
– Iteration: for $i = 1, \dots, m$, $k = 1, \dots, N$, $n = 0, 1, 2, \dots$

$$c_k^{n+1} = \frac{\int_\Omega I M_k^n dx}{\int_\Omega M_k^n dx},$$

$$u_i^{n+1} = \min\left\{\max\left\{\frac{1}{4}(u_i^{so,n} + u_i^{no,n} + u_i^{ea,n} + u_i^{we,n} - \lambda r_i^n), 0\right\}, 1\right\}.$$

– Termination criterion:

$$\|c^{n+1} - c^n\| \le \epsilon.$$

4 Extension to Other Distance Functions

In the above modeling and analysis, we assume the distance function be $d_k = (I - c_k)^2$. In fact, the above framework of solving $\mathbf{U}(\mathbf{V})$ is adapted to general distance functions. The changed part is only the region variables in distance function. However, the region variables are easy to solve since they are only involved in the distance terms in the energy. In the following, we list the distance functions adapted to piecewise smooth images, texture images and vector-valued images.

4.1 Piecewise Smooth Images

We assume the piecewise smooth images can be approximated by the product of a piecewise constant image and a smooth function. That is

$$I(x) \approx b(x) \left(\sum_{k=1}^{N} c_k \mathbf{1}_{D_k}(x) \right), \tag{35}$$

where b is a smooth function. This assumption is satisfied at least by medical images where intensity inhomogeneity often occurs from different modalities, such as X-ray radiography/tomography and magnetic resonance images. Intensity inhomogeneity is called bias field represented by $b(x)$ in (35). The bias field causes serious errors when using piecewise constant models such as Chan-Vese model or the proposed models with $d_k = (I - c_k)^2$. To handle the smoothness of bias field, [15] assumed that

$$b(x) = \sum_{i=1}^{l} w_j G_j(x),$$

that is, the bias field is a linear combination of some known polynomial basis functions $G = (G_1, \dots, G_l)$, and proposed the following distance function

$$d_k = (I - bc_k)^2. \tag{36}$$

However, since there is no regularization technique in [15], the method is sensitive to noise.

To overcome this drawback, we can consider total variation regularization or H^1 regularization on membership functions. That is equivalent to using the distance term (36) in our proposed segmentation framework. In [15], it has been shown that $\mathbf{w}$ (and thus b) and c_k have closed-form solutions

$$c_k = \frac{\int_\Omega I b M_k dx}{\int_\Omega b^2 M_k dx},$$

$$\mathbf{w} = A^{-1}\mathbf{v},$$

where

$$A = \int_\Omega \mathbf{G}\mathbf{G}^T \left(\sum_{k=1}^{N} c_k M_k \right)^2 dx,$$

$$\mathbf{v} = \int_\Omega \mathbf{G} I \left(\sum_{k=1}^{N} c_k M_k \right) dx.$$

Hence the algorithm for piecewise smooth image segmentation can be obtained by updating c_k by the new formula and adding a step of updating weight $\mathbf{w}$ in the alternating iterative algorithms in Sect. 3.

4.2 Texture Images

For texture images, we choose to work on the probability density function (pdf) but not the image intensity since the consistency of texture can be well described by statistics like pdf. Here we adopt the distance function introduced in region competition model [29]. Assume the pdf in region D_k is $P_k(x)$, then the distance function is given by

$$d_k(x) = -\log P_k(I(x)). \tag{37}$$

However, a parametric Gaussian pdf is used in [29]. Here we note that a non-parametric pdf is better for texture image. In this paper, the pdf $P_k(I(x))$ in region D_k is estimated by Parzen window method in which the samples are the intensities $\{I(x), x \in D_k\}$. Parzen window method is a non-parametric kernel density estimation method. See [22] for more details. Then the algorithm for texture image segmentation can be obtained by replacing the updating of c_k by updating $P_k(x)$ in the algorithms in Sect. 3.

4.3 Vector-Valued Images

We use the simplest one defined based on each channel. Assume $\mathbf{I} : \Omega \to \mathbb{R}^p$ be the vector-valued image, we define the distance at each gray image I_l as d_{kl}, $l = 1, \dots, p$ by one of the above mentioned methods. Then we can define the distance d_k for vector-valued image I as

$$d_k = \frac{1}{p} \sum_{l=1}^{p} d_{kl}. \tag{38}$$

All the involved region variables (if there are any) can be solved as above for each gray image $I_l, l = 1, \dots, p$.

For instance, the Chan-Vese distance term for vector-valued image $\mathbf{I}$ is defined as

$$d_k(\mathbf{I}, \mathbf{c}_k) = \frac{1}{p} \sum_{l=1}^{p} d_{kl}(I_k, c_{kl}), \tag{39}$$

where

$$d_{kl}(I_k, c_{kl}) = (I_k - c_{kl})^2,$$

and $\mathbf{c}_k = (c_{k1}, \dots, c_{kp})$. It is easy to derive the formula of c_{kl}, which is

$$c_{kl} = \frac{\int_\Omega I_k(x) u_l^p(x) dx}{\int_\Omega u_l^p(x) dx}.$$

Then the algorithm for vector-valued image segmentation can be obtained by using the new formulas of c_k and d_k in the algorithms in Sect. 3.

5 Experimental Results

We tested our algorithm on piecewise constant images, piecewise smooth MR images and texture images. Both gray scale and color images are tested. We choose different distance terms for different kinds of images. Some parameters are fixed as follows: $\theta = 0.1$, $\tau = 0.1$, $\epsilon = 10^{-4}$. The parameter λ is required to be tuned for each image. The default initialization of membership functions is: $u_1^0 = I / \max_\Omega(I)$, u_i^0 $(i = 2, \dots, m)$ be random matrices follow uniform distribution at [0, 1]. For texture images in Fig. 6(a), special initialization is required for good result. We draw m circles on the image and set the membership function $u_i^0 = 1$ $(i = 1, \dots, m)$ inside the circle and $u_i^0 = 0$ $(i = 1, \dots, m)$ outside. In all the experiments, the final segmentation results are obtained by checking the class where its membership function value at the pixel is the largest among all membership functions. The experiments are performed under Windows XP and MATLAB v7.4 with Intel Core 2 Duo CPU at 1.66 GHz and 2 GB memory.

5.1 Gray Scale Cartoon Image Segmentation

In Fig. 1, we compare the Chan-Vese level set method and our methods with TV and H^1 regularization. The solutions of the three methods are displayed in Fig. 1(b)–(d). In Fig. 1(b), the contours of zero level sets ($\phi_1 = 0$, $\phi_2 = 0$) are displayed in red and green color. In Fig. 1(c)–(d), the contours of $u_1 = 0.5$ and $u_2 = 0.5$ are displayed. Although in our methods we allow the membership functions valued between 0 and 1, in this example, we observe that the final $u_1, u_2, M_1, M_2, M_3, M_4$ in the proposed two methods are in fact characteristic functions valued as 0 and 1. Numerically, we can check that $u_1 = H(\phi_1)$, $u_2 = H(\phi_2)$, $M_1 = H(\phi_1)H(\phi_2)$, $M_2 = H(\phi_1)(1 - H(\phi_2))$, $M_3 = (1 - H(\phi_1))H(\phi_2)$, $M_4 = (1 - H(\phi_1))(1 - H(\phi_2))$ where ϕ_1, ϕ_2 are the level set functions in Chan-Vese method, and so the three methods give the same solution. Our methods converge with less computational time than Chan-Vese method. We remark that although we use four-phase segmentation model ($N = 4$), the final segmentation contains three meaningful phases (Fig. 1(e)–(g), Fig. 1(i)–(k) and Fig. 1(m)–(o)) and one empty phase (Fig. 1(h), Fig. 1(l) and Fig. 1(p)). We also remark that the proposed models with $N = 3$ give the same meaningful phases.

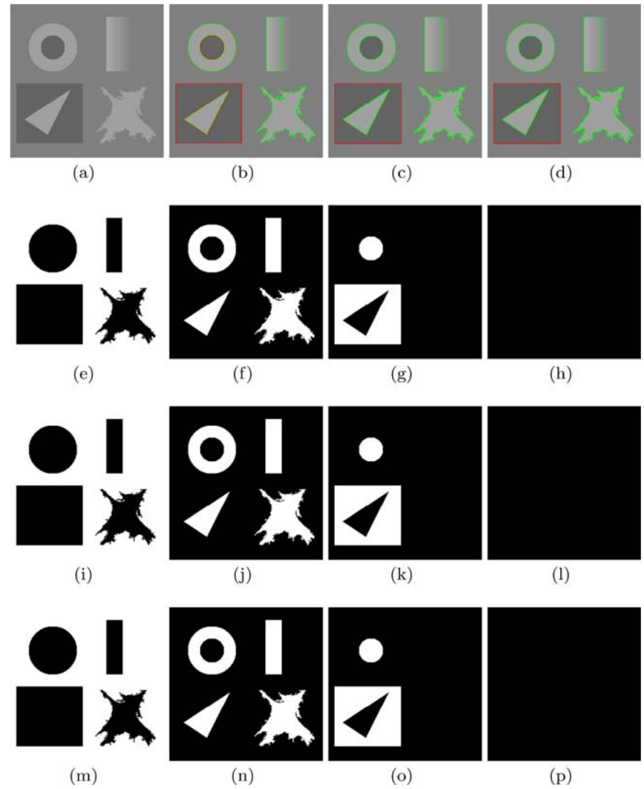

Fig. 1 Comparison of the Chan-Vese level set method and the proposed methods with four-phase segmentation. (**a**) the test image; (**b**) the segmentation by Chan-Vese method [$\lambda = 1$, computational time = 2.1 seconds, number of iterations = 12]; (**c**) the segmentation by the proposed method with TV regularization [$\lambda = 10$, computational time = 0.5 seconds, number of iterations = 7]; (**d**) the segmentation by the proposed method with H^1 regularization [$\lambda = 10$, computational time = 0.2 seconds, number of iterations = 6]; (**e**)–(**h**) the four phases by the Chan-Vese method; (**i**)–(**l**) the membership functions $M_1, \dots, M_4$ by the proposed method with TV regularization; (**m**)–(**p**) the membership functions $M_1, \dots, M_4$ by the proposed method with H^1 regularization

In Fig. 2, we compare the piecewise constant level set method (PCLSM) in [16] and our methods with TV and H^1 regularization. Both of our methods give better segmentation results (in which each class is indicated by one color) with less computational time than PCLSM method. Among them, our method with TV regularization gives the best segmentation result in Fig. 2(d), and our method with H^1 regularization consumes the shortest time. The phases and membership functions of all the three methods are displayed in the last three rows. We get that the PCLSM gives almost hard phases valued as 0 and 1 while our methods give soft membership functions valued between [0, 1].

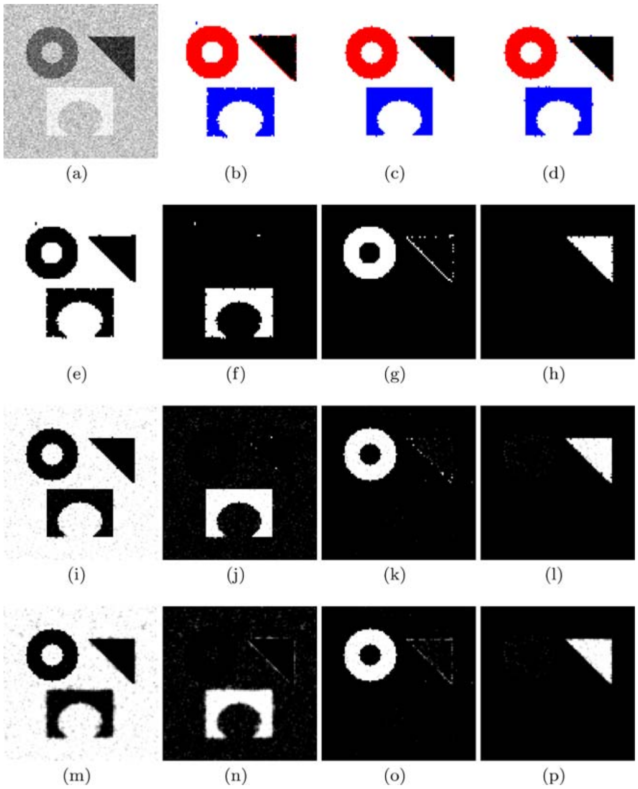

Fig. 2 Comparison of the PCLSM method and the proposed methods with four-phase segmentation. (**a**) the noisy test image; (**b**) the segmentation by PCLSM method [computational time = 76.2 seconds]; (**c**) the segmentation by the proposed method with TV regularization [$\lambda = 0.0008$, computational time = 1.9 seconds]; (**d**) the segmentation by the proposed method with H^1 regularization [$\lambda = 0.0003$, computational time = 0.4 seconds]; (**e**)–(**h**) the four phases by the PCLSM method; (**i**)–(**l**) the membership functions $M_1, \ldots, M_4$ by the proposed method with TV regularization; (**m**)–(**p**) the membership functions $M_1, \ldots, M_4$ by the proposed method with H^1 regularization

In Fig. 3, we compare the performance of our methods with TV and H^1 regularization on a synthetic image with different noise levels. The first row in Fig. 3 gives the images contaminated by Gaussian noise with standard deviation 15, 20, 25 and 30. The second and third rows show the segmentation results by TV regularization and H^1 regularization respectively, and each column corresponds to one noise level. In order to quantify the segmentation results, we use segmentation accuracy which is defined as the ratio of the number of rightly classified pixels and the total number of pixels. Table 1 demonstrates the performance of the two methods includes computational time, iteration and segmentation accuracy. We can conclude from Table 1 that H^1 regularization consumes less time in each case. In the aspect of segmentation accuracy, TV regularization has higher accuracy than H^1 regularization when the noise standard deviation is 15, however, as the noise increased, H^1 regularization has higher accuracy. It shows that H^1 regularization is more robust to noise than TV regularization.

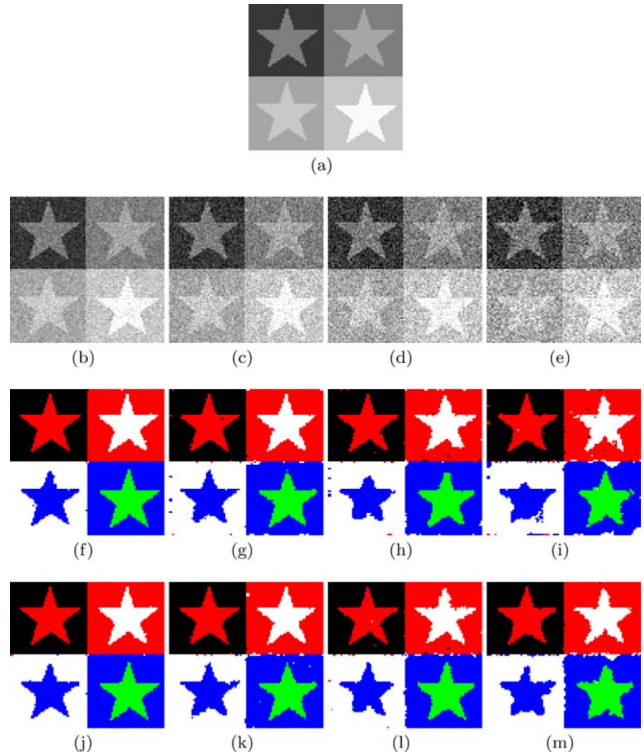

Fig. 3 Comparison of the proposed methods on different noise levels. (**a**) the clean piecewise constant image; (**b**)–(**e**) images contaminated by zero mean Gaussian noise with standard device 15, 20, 25 and 30 respectively; (**f**)–(**i**) the classification results of the proposed model with TV regularization corresponding to (**b**)–(**e**) with $\lambda = 0.001, 0.0007, 0.0005, 0.00045$ respectively; (**j**)–(**m**) the classification results of the proposed model with H^1 regularization corresponding to (**b**)–(**e**) with $\lambda = 0.0006, 0.0004, 0.0003, 0.0002$ respectively

Table 1 The performance of TV regularization vs H^1 regularization

Regularization method	Noise standard device	Iterations	Computational time	Classification accuracy
TV	15	85	1.35 s	99.42%
	20	133	1.76 s	98.31%
	25	174	2.72 s	97.28%
	30	206	3.21 s	95.24%
H^1	15	67	0.34 s	99.36%
	20	128	0.71 s	98.44%
	25	174	0.82 s	97.63%
	30	329	1.96 s	96.11%

5.2 Brain MR Image Segmentation

For brain MR images, we use the distance function (36). In Fig. 4, we use our method with TV regularization. Figure 4(b) is the bias corrected image obtained by I/b. The

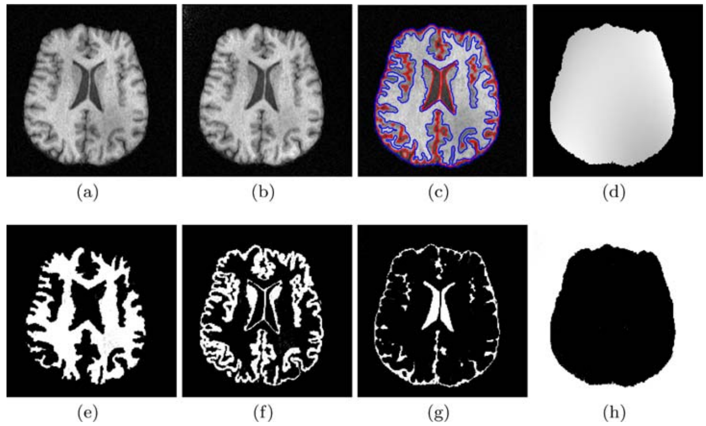

Fig. 4 Four-phase segmentation of a real brain MRI image by TV regularization. (**a**) the noisy MRI image; (**b**) the bias corrected image; (**c**) the segmentation result, $\lambda = 0.0015$; (**d**) the estimated bias field; (**e**)–(**h**) the membership functions $M_1, \ldots, M_4$

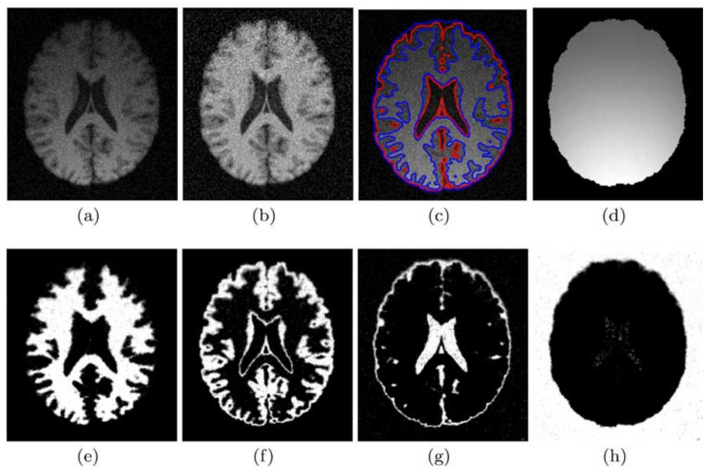

Fig. 5 Four-phase segmentation of a brain MRI image with noise 9% by H^1 regularization. (**a**) the noisy MRI image; (**b**) the bias corrected image; (**c**) the segmentation result, $\lambda = 0.001$; (**d**) the estimated bias field; (**e**)–(**h**) the membership functions $M_1, \ldots, M_4$

segmentation result is showed in Fig. 4(c) by red and blue contours. Figure 4(d) shows the estimated bias field which is smooth. The membership functions in Fig. 4(e)–(h) corresponds to the white matter (WM), gray matter (GM), cerebrospinal fluid (CSF) and the background. The results are satisfactory.

In Fig. 5, a brain MR image with serious intensity inhomogeneity and with simulated noise 9% is tested by our method with H^1 regularization. The bias corrected image in Fig. 5(b), the segmentation in Fig. 5(c) and the estimated bias field in Fig. 5(d) are good. The membership functions $M_1, \ldots, M_4$ in Fig. 5(e)–(h) correspond to WM, GM, CSF and background respectively.

5.3 Texture Image Segmentation

We use the distance function (37) for texture image segmentation. Figure 6 gives a three phase segmentation example. Both TV and H^1 regularization are tested. Though the membership functions of the two methods (the second row is for TV, the third row is for H^1) seem something different, the final maximum membership segmentation results in Fig. 6(b)–(c) are similar and satisfactory.

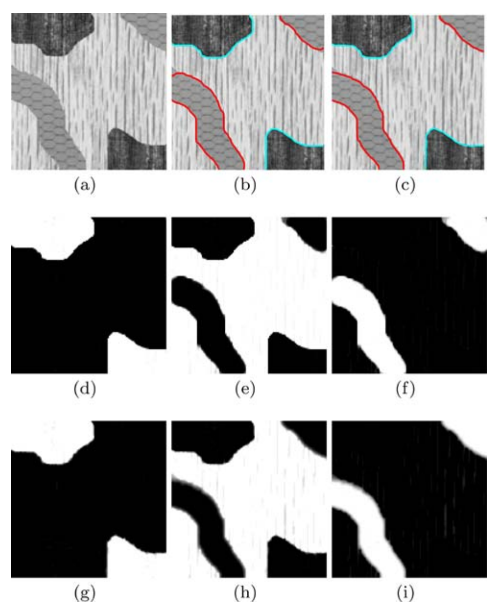

Fig. 6 Three-phase segmentation of a texture image. (**a**) the texture image; (**b**) the segmentation result by TV regularization, $\lambda = 0.2$; (**c**) the segmentation result by H^1 regularization, $\lambda = 0.0001$; (**d**)–(**f**) the membership functions $M_1, \ldots, M_3$ by TV regularization; (**g**)–(**i**) the membership functions $M_1, \ldots, M_3$ by H^1 regularization

Figure 7 gives a texture image with five-phase segmentation. Special initialization of membership functions are used as in Fig. 7(a). The results of TV in Fig. 7(b)–(c) and the results of H^1 regularization in Fig. 7(d)–(e) are competitive and satisfactory. The membership functions of TV and H^1 regularization are displayed in the second and the third rows respectively.

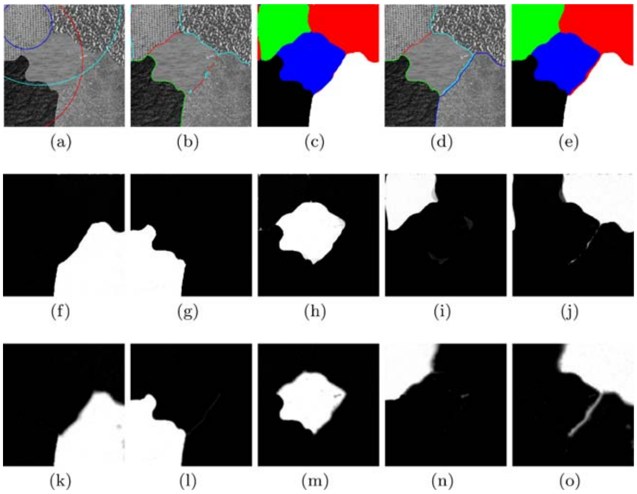

Fig. 7 Five-phase segmentation of a texture image: (**a**) the texture with initialization circles; (**b**)–(**c**) the segmentation results by TV regularization, $\lambda = 0.12$; (**d**)–(**e**) the segmentation results by H^1 regularization, $\lambda = 0.03$; (**f**)–(**j**) the membership functions $M_1, \ldots, M_5$ by TV regularization; (**k**)–(**o**) the membership functions $M_1, \ldots, M_5$ by H^1 regularization

5.4 Color Image Segmentation

For color image, we use the distance function in (39). Figures 8 and 9 display the results of two color images with four and six phase segmentation.

In Fig. 8, we compare our methods with Chan-Vese level set method. For the four-phase Chan-Vese model, two level sets ϕ_1, ϕ_2 are needed. Figures 8(b) and 8(c) display the initial and the final zero level sets. Figure 8(d) shows the piecewise constant image given by formula $\sum_{i=1}^{4} c_i \chi_{\Omega_i}$ where χ_{Ω_i} are the characteristic functions of the following four regions: $\Omega_1 = \{x|\phi_1(x) \geq 0, \phi_2(x) \geq 0\}$, $\Omega_2 = \{x|\phi_1(x) \geq 0, \phi_2(x) < 0\}$, $\Omega_3 = \{x|\phi_1(x) < 0, \phi_2(x) \geq 0\}$, $\Omega_4 = \{x|\phi_1(x) < 0, \phi_2(x) < 0\}$. Figures 8(e)–(f) are the initialization of the proposed methods. It is obvious that our segmentation results in Fig. 8(g) (by TV regularization) and Fig. 8(h) (by H^1 regularization) are more accurate than the result in Fig. 8(d). We also compare the computational times of the three methods. Our algorithm with H^1 regularization

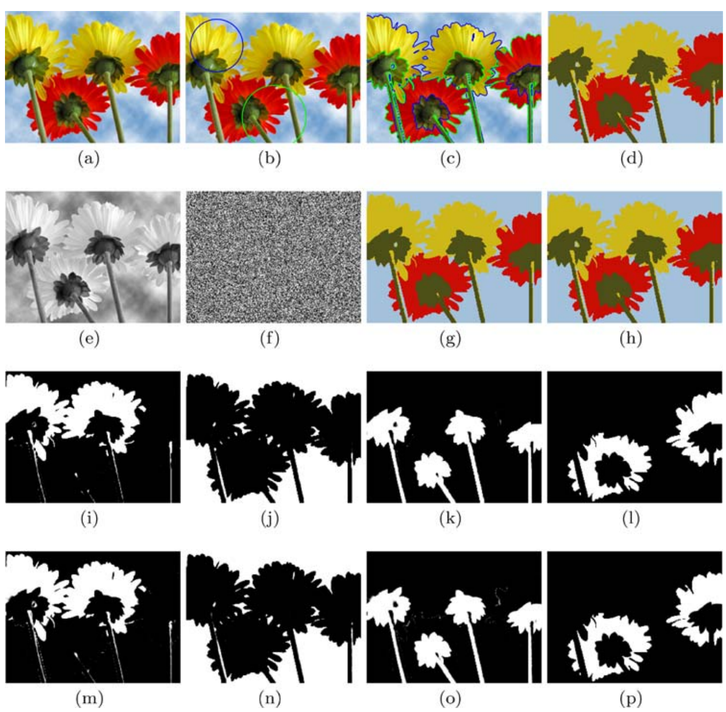

Fig. 8 Comparison of the Chan-Vese level set method and the proposed two methods. (**a**) the test color image; (**b**) the initial zero level sets by the Chan-Vese method; (**c**) the final zero level sets by the Chan-Vese method; (**d**) the piecewise constant segmentation by the Chan-Vese method [$\lambda = 0.01$, computational time $= 14.5$ seconds, number of iterations $= 100$]; (**e**)–(**f**) initial u_1 and u_2 in our methods; (**g**) the piecewise constant segmentation by TV regularization [$\lambda = 0.0004$, computational time $= 5.2$ seconds, number of iterations $= 58$]; (**h**) the piecewise constant segmentation by H^1 regularization [$\lambda = 0.0005$, computational time $= 3.0$ seconds, number of iterations $= 35$]; (**i**)–(**l**) the membership functions $M_1, \ldots, M_4$ by TV regularization; (**m**)–(**p**) the membership functions $M_1, \ldots, M_4$ by H^1 regularization

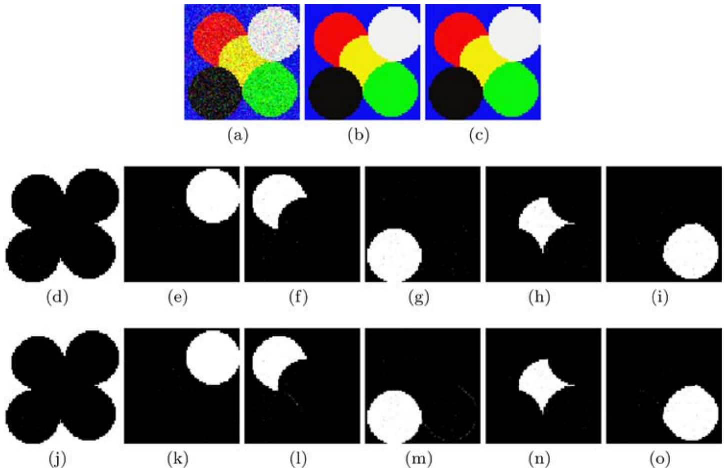

Fig. 9 Six-phase color image segmentation by TV and H^1 regularization. (**a**) the noisy image contaminated by zero mean Gaussian noise with standard device 50; (**b**) the piecewise constant segmentation by TV regularization, $\lambda = 0.0003$; (**c**) the piecewise constant segmentation by H^1 regularization, $\lambda = 0.0001$; (**d**)–(**i**) the membership functions $M_1, \ldots, M_6$ by TV regularization; (**j**)–(**o**) the membership functions $M_1, \ldots, M_6$ by H^1 regularization

is the fastest among the three which takes 3.0 seconds while Chan-Vese level set method is the slowest which takes 15.2 seconds. Remark that in our implementation of Chan-Vese model, in order to make the Chan-Vese algorithm more efficient, we use $|\nabla \phi_i|$ instead of $\delta_\epsilon(\phi_i)$ in the evolution equations. The membership functions of TV and H^1 regularization are displayed in the second and the third rows respectively.

In Fig. 9, we test a synthetic image Fig. 9(a) contaminated by zero mean Gaussian noise with standard deviation 50. Figures 9(b) and 9(c) show the piecewise constant segmentation results of the test image by our methods with TV and H^1 regularization which are satisfactory. The corresponding membership functions of TV and H^1 regularization are displayed in the second and the third rows respectively.

6 Conclusion

Inspired by the level set formulation of multiphase Chan-Vese model, we have proposed a variational soft segmentation framework. We have designed a general representation of regions by soft membership functions which automatically satisfies the sum to one constraint. To ensure the smoothness of membership, both TV regularization and H^1 regularization are considered. The two regularization methods have their own advantages. Fast numerical schemes are designed for the two regularization methods. By changing the distance function, the proposed segmentation framework can be easily extended such that we can handle different kinds of images. Numerical results on cartoon images, piecewise smooth images and texture images are promising.

Mathematically, our methods are relaxations of Chan-Vese method which enlarged the solution space, so we can hope that in some cases our methods and Chan-Vese method would give the same solution. Figure 1 is such an example. In the future work, we will make a more insightful comparison between these models, both from a purely mathematical point of view (i.e. proving when they provide the same solution) and from an experimental point of view, and we will also study the convergence of the numerical algorithms.

Acknowledgements The authors would like to thank Prof. X.-C. Tai and E. Bae for providing the result of PCLSM method in Figure 2. This work is partially supported by the National Science Foundation of Shanghai (10ZR1410200), the National Science Foundation of China (60773119) and the Research Fund for the Doctoral Program of Higher Education (No. 200802691037).

Appendix

Proof of Proposition 1 The problem (26) is a convex program (CP) problem which admits a unique global minimizer. Assume $\bar{U}^* = (u_1^*, \ldots, u_m^*)$ is the unique solution of (26), then the following Karush-Kuhn-Tucker (KKT) conditions [14] are both necessary and sufficient:

(a) $u_i^*(x) \ge 0$, $1 - u_i^*(x) \ge 0$
(b) There exist Lagrange multipliers $\beta_i^*(x)$ and $\gamma_i^*(x)$ for each point $x \in \Omega$ such that

$$\frac{\partial F(U)}{\partial u_i^*(x)} = \frac{1}{\theta}(u_i^*(x) - v_i(x)) + \lambda r_i(x) = \beta_i^*(x) - \gamma_i^*(x)$$

(c) $\beta_i^*(x) u_i^*(x) = 0$, $\gamma_i^*(x)(1 - u_i^*(x)) = 0$

(d) $\beta_i^*(x) \ge 0$, $\gamma_i^*(x) \ge 0$

for $i = 1, \ldots, m$.

Define $\eta_i(x) = \frac{1}{\theta}(u_i(x) - v_i(x)) + \lambda r_i(x)$ and $\hat{\eta}_i(x) = \frac{1}{\theta}(\hat{u}_i(x) - v_i(x)) + \lambda r_i(x)$. Since u_i satisfies (30), we have $\eta_i(x) = 0$. For each $x \in \Omega$, we choose $\hat{\beta}_i(x)$ and $\hat{\gamma}_i(x)$ as follows:

If $\hat{u}_i(x) \in (0, 1)$, then $u_i(x) \in (0, 1)$ and $u_i(x) = \hat{u}_i(x)$, hence $\hat{\eta}_i(x) = \eta_i(x) = 0$. Set $\hat{\beta}_i(x) = 0$ and $\hat{\gamma}_i(x) = 0$;

If $\hat{u}_i(x) = 0$, then $u_i(x) \leq 0$ and $\hat{u}_i(x) \geq u_i(x)$, hence $\hat{\eta}_i(x) \geq \eta_i(x) = 0$. Set $\hat{\beta}_i(x) = \hat{\eta}_i(x)$ and $\hat{\gamma}_i(x) = 0$;

If $\hat{u}_i(x) = 1$, then $u_i(x) \geq 1$ and $\hat{u}_i(x) \leq u_i(x)$, hence $\hat{\eta}_i(x) \leq \eta_i(x) = 0$. Set $\hat{\beta}_i(x) = 0$ and $\hat{\gamma}_i(x) = -\hat{\eta}_i(x)$.

It is easy to verify that $\{\hat{u}_i, \hat{\beta}_i, \hat{\gamma}_i\}$ satisfies KKT conditions (a)–(d). Therefore $\hat{U}$ is a minimizer of problem (26) and by uniqueness $U^* = \hat{U}$. Hence we conclude that $\hat{U}$ is the exact closed-form solution of problem (26). □

References

1. Bezdek, J.C., Hall, L.O., Clarke, L.P.: Review of MR image segmentation techniques using pattern recognition. Med. Phys. **20**, 1033–1048 (1993)
2. Bresson, X., Esedoglu, S., Vandergheynst, P., Thiran, J.-P., Osher, S.: Fast global minimization of the active contour/snake model. J. Math. Imaging Vis. **28**(2), 151–167 (2007)
3. Caselles, V., Kimmel, R., Sapiro, G.: Geodesic active contours. Int. J. Comput. Vis. **1**, 61–79 (1997)
4. Chan, T.F., Vese, L.A.: Active contour without edges. IEEE Trans. Image Process. **10**, 266–277 (2001)
5. Chan, T., Sandberg, B., Vese, L.: Active contours without edges for vector-valued images. J. Vis. Commun. Image Represent. **11**, 130–141 (2000)
6. Chan, T.F., Esedoglu, S., Nikolova, M.: Algorithms for finding global minimizers of image segmentation and denoising models. SIAM J. Appl. Math. **66**, 1632–1648 (2006)
7. Chambolle, A.: An algorithm for total variation minimization and applications. J. Math. Imaging Vis. **20**(1–2), 89–97 (2004)
8. Goldstein, T., Osher, S.: The split Bregman method for L1 regularized problems. UCLA CAAM Report 08-29
9. Goldstein, T., Bresson, X., Osher, S.: Geometric applications of the split Bregman method: segmentation and surface reconstruction. UCLA CAAM Report 09-06
10. Houhou, N., Thiran, J.P., Bresson, X.: Fast texture segmentation model based on the shape operator and active contour. In: IEEE Conference on Computer Vision and Pattern Recognition, CVPR 2008 (2008)
11. Jia, R.-Q., Zhao, H.: A fast algorithm for the total variation model of image denoising. Adv. Comput. Math. (2009). doi:10.1007/s10444-009-9128-5
12. Jung, Y., Kang, S., Shen, J.: Multiphase image segmentation via Modica-Mortola phase transition. SIAM J. Appl. Math. **67**, 1213–1232 (2007)
13. Kass, M., Witkin, A., Tetzopoulos, D.: Snakes: Active contour models. Int. J. Comput. Vis. **1**, 321–331 (1988)
14. Kuhn, H.W., Tucker, A.W.: Nonlinear programming. In: Proceedings of 2nd Berkeley Symposium, pp. 481–492. University of California Press, Berkeley (1951)
15. Li, C., Gatenby, C., Wang, L., Gore, J.C.: A robust parametric method for bias field estimation and segmentation of MR images. In: IEEE Conference on Computer Vision and Pattern Recognition, CVPR2009, pp. 218–223
16. Lie, J., Lysaker, M., Tai, X.-C.: A binary level set model and some applications to Mumford-Shah image segmentation. IEEE Trans. Image Process. **15**, 1171–1181 (2006)
17. Mory, B., Ardon, R.: Fuzzy region competition: a convex two-phase segmentation framework. In: Sgallari, F., Murli, A., Paragios, N. (eds.) SSVM 2007. LNCS, vol. 4485, pp. 214–226. Springer, Berlin (2007)
18. Mory, B., Ardon, R.: Variational segmentation using fuzzy region competition and local non-parametric probability density functions. In: IEEE 11th International Conference on Computer Vision, ICCV 2007, pp. 1–8 (2007)
19. Mumford, D., Shah, J.: Optimal approximations by piecewise smooth functions and associated variational problems. Commun. Pure Appl. Math. **42**, 577–685 (1989)
20. Osher, S., Paragios, N., Geometric Level, Set: Methods in Imaging Vision and Graphics. Springer, Berlin (2003)
21. Paragios, N., Deriche, R.: Geodesic active regions for supervised texture segmentation. In: Proceedings of International Conference on Computer Vision, pp. 22–25 (1999)
22. Parzen, E.: On the estimation of a probability density function and mode. Ann. Math. Stat. **33**, 1065–1076 (1962)
23. Rudin, L., Osher, S., Fatemi, E.: Nonlinear total variation based noise removal algorithms. Physica D **60**, 259–268 (1992)
24. Sethian, J.A.: Level Set Methods: Evolving Interfaces in Geometry, Fluid Mechanics, Computer Vision and Materials Sciences. Cambridge University Press, Cambridge (1996)
25. Shen, C.M.: Geometric variational principle based image processing method. PhD thesis of East China Normal Univ. (2009) (in Chinese)
26. Shen, J.: A stochastic-variational model for soft Mumford-Shah segmentation. Int. J. Biomed. Imaging **2006**, 1–14 (2006)
27. Vese, L.A., Chan, T.F.: A multiphase level set framework for image segmentation using the Mumford and Shah model. Int. J. Comput. Vis. **50**(3), 271–293 (2002)
28. Vovk, U., Pernus, F., Likar, B.: A review of methods for correction of intensity inhomogeneity in MRI. IEEE Trans. Med. Imaging **26**(3), 405–421 (2007)
29. Zhu, S.C., Yuille, A.: Region competition: unifying snakes, region growing, and Bayes/mdl for multiband image segmentation. IEEE Trans. Pattern Anal. Mach. Intell. **18**, 884–900 (1996)

Fang Li received her MSc degree in Mathematics from the South West China Normal University in 2004 and she received her Ph.D. degree in Mathematics from the East China Normal University in 2007. She is currently a lecturer in the Department of Mathematics, East China Normal University. Her research interests include anisotropic diffusion filtering, the variational methods and PDEs in image processing.

Chaomin Shen is a lecturer of computer science at East China Normal University (ECNU). He received his Ph.D. and Master degrees from ECNU and the National University of Singapore (NUS) respectively, all in Mathematics. During 1998 and 2004, he was with the Centre for Remote Imaging, Sensing and Processing (CRISP), NUS, as an associate scientist. His research interest is image processing using mathematical methods.

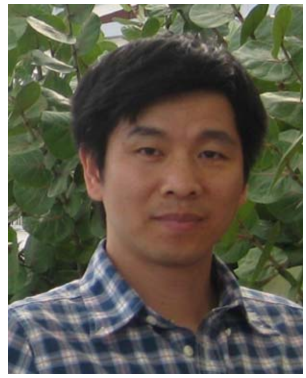

Chunming Li received the Ph.D. degree in Electrical Engineering from University of Connecticut, Storrs, CT, in 2005. Between 2001 and 2003, he was a consultant for Robotics Technology Group, ABB Corporate Research, where he worked on image processing and camera calibration algorithms. From 2003 to 2005, he did his Ph.D. research on medical image processing and analysis, which was supported by Pfizer Global Research and Development. He is currently a research fellow at Vanderbilt University Institute of Imaging Science. His research interests include the development and application of algorithms in image processing, medical imaging, and computer vision.